

Article

A Distributed Control Strategy for Islanded Single-Phase Microgrids with Hybrid Energy Storage Systems Based on Power Line Signaling

Pablo Quintana-Barcia ^{1,*} , Tomislav Dragicevic ², Jorge Garcia ¹ , Javier Ribas ¹ and Josep M. Guerrero ² 

¹ ce3i2 Group, Department of Electrical Engineering, University of Oviedo, 33204 Gijon, Spain; garciajorge@uniovi.es (J.G.); ribas@uniovi.es (J.R.)

² Department of Energy Technology, Aalborg University, 9920 Aalborg, Denmark; tdr@et.aau.dk (T.D.); joz@et.aau.dk (J.M.G.)

* Correspondence: quintanapablo@uniovi.es; Tel.: +34-985-18-2557

Received: 11 December 2018; Accepted: 22 December 2018; Published: 28 December 2018



Abstract: Energy management control is essential to microgrids (MGs), especially to single-phase ones. To handle the variety of distributed generators (DGs) that can be found in a MG, e.g., renewable energy sources (RESs) and energy storage systems (ESSs), a coordinated power regulation is required. The latter are generally battery-based systems whose lifetime is directly related to charge/discharge processes, whereas the most common RESs in a MG are photovoltaic (PV) units. Hybrid energy storage systems (HESS) extend batteries life expectancy, thanks to the effect of supercapacitors, but they also require more complex control strategies. Conventional droop methodologies are usually applied to provide autonomous and coordinated power control. This paper proposes a method for coordination of a single-phase MG composed by a number of sources (HESS, RES, etc.) using power line signaling (PLS). In this distributed control strategy, a signal whose frequency is higher than the grid is broadcasted to communicate with all DGs when the state of charge (*SoC*) of the batteries reaches a maximum value. This technique prevents batteries from overcharging and maximizes the power contribution of the RESs to the MG. Moreover, different commands apart from the *SoC* can be broadcasted, just by changing to other frequency bands. The HESS master unit operates as a grid-forming unit, whereas RESs act as grid followers. Supercapacitors in the HESS compensate for energy peaks, while batteries respond smoothly to changes in the load, also expanding its lifetime due to less aggressive power references. In this paper, a control structure that allows the implementation of this strategy in single-phase MGs is presented, with the analysis of the optimal range of PLS frequencies and the required self-adaptive proportional-resonant controllers.

Keywords: active power control; energy storage; hybrid; microgrid; photovoltaic; power-line signaling; renewable energy sources; single-phase

1. Introduction

Power systems of today and those developed more than a century ago have several points in common. Firstly, they consist of large power plants installed far away from consumption points. Power flows are unidirectional, moving through long, expensive transmission lines and their operation is demand-driven. These power systems are exceptionally complex and require reliable control strategies to ensure the quality of the grid [1–3]. In the last few decades, this concept has been continuously evolving thanks to modern solutions such as distributed generators DGs—primarily based on energy storage systems (ESSs) and renewable energy sources (RESs)—active demand management combined

with smart control, and the introduction of new communication technologies (ITCs) [4,5]. Researchers have been seeking a robust and trustworthy solution that integrates ESSs, RESs and loads into small power systems. This is what has pushed the emergence of the microgrid (MG) concept [1,3–6].

A popular solution today is a DC MG, due to the fact that there is no need for synchronization and the non-existence of reactive power. However, AC MGs are still a valid and reliable solution [3]. They can be operated either in grid-connected (exchanging power with the mains) or islanded (supporting local loads if the grid is not present) modes, although these changes must be seamless and swift, avoiding undesirable transients [7].

In recent years, photovoltaic (PV) unit installation costs have decreased dramatically, and this technology has become one of the major DGs meant to supply MGs. Small wind turbines are also beginning to carve a niche in the market, albeit more slowly [7–10]. However, due to the stochastic nature of renewable energies, ESSs are essential elements for balancing power flows between RESs and loads in islanded MGs [3,11,12]. Moreover, a master ESS works as a grid-forming unit, generating the same AC grid conditions as conventional power systems, whereas renewable sources usually operate as grid-following systems, injecting all their available power into the MG [5,13]. Conventional ESS also has the role of power balance and frequency stability by absorbing or injecting a current from its power source, i.e., batteries. This concept implies that the capacity limitation of these electrochemical devices must be considered in the studies, and to preserve their lifetime, avoiding frequent deep discharge cycles is crucial. The state of charge (SoC) of the batteries needs to be kept, therefore, in a safe region in order not to damage the devices [14,15]. This is why the hybrid energy storage system (HESS) is becoming an interesting solution, able to extend batteries' useful life. By combining fast-dynamics high-power storage devices as supercapacitors and ultracapacitors with bulk-energy electrochemical units, the performance of classic grid forming ESSs has been improved [16–19]. The initial investment in supercapacitors can be paid off by extending the useful life of the batteries. In this work, the master HESS consists of a battery energy storage system (BESS) plus a supercapacitor energy storage system (SESS).

On the other hand, classic MGs are based on three-phase systems. The advantages of three-phase systems are well known: power delivered is constant, transmission of power requires less conductor material, they exhibit good stability and reliability, etc. Single-phase AC needs more capacitance in the DC link than three-phase, typically electrolytic capacitors that used to reduce lifetime. However, electrolytic capacitors' reliability has increased over the past years and now they are not as critical as they used to be [20]. The key to making them last longer is to have them working under their maximum operating temperature [21–24]. On the other hand, it is a fact that most buildings are single-phase supplied. This implies that a small community of neighbors with a certain number of renewable elements (PV panels) and batteries can become a single-phase MG just by adding some sort of control: the most popular and well-known kind of control of a MG is a centralized structure. All functionalities can be integrated into a MG's central controller, which makes decisions based on the measurements from the sensors all over the power system. After processing the data, the central controller sends instructions to the elements that form the MG through some kind of communications system, e.g., wireless, droop algorithms, wired connection, etc. This offers good control capability, but if the number of units increases, their connectivity may require extensive hardware. In addition, the reliability of the whole system depends on one key element [25,26]. Droop control strategy (using frequency deviation of each unit to distribute active power) is widely accepted to fit into this requirement. However, the active power distribution is based on a unified local control algorithm, which ignores the inherent power regulation difference between the ESS and the RESs [27].

In order to tackle this issue and avoid using external communications, a power line can be employed. This technique provides a distributed control using the MG's own power lines as an interface. Signals travel along these carriers with a certain frequency, providing significant information to all the units that form the MG. However, this implies an introduction of noise and therefore, the bandwidth of these signals must be properly designed [28–32]. Previous works have employed

similar techniques for islanded DC or three-phase AC microgrids, control of parallel inverters, and more. However, in the particular case of this work, the BESS generates a power line signal (PLS) that informs the RESs distributed along the single-phase MG to reduce their power contribution, due to the fact that the batteries are reaching their maximum *SoC*. The frequency of this signal is proportional to the *SoC* of the batteries. However, below a certain *SoC*, the PLS is turned off and all the grid-followers operate at their nominal operation point. Additional PLS triggers may be programmed, e.g., protection against huge derivatives of batteries' input current, due to extreme sudden changes in the load, a reactive power command, etc. This flexible solution avoids using centralized control or droop strategies and hence, there is no need for secondary control of the frequency.

This paper is organized as follows: in Section 2, the physical configuration of the MG is presented. Section 3 describes the PLS concept and how it can be applied to single-phase MGs. The energy management strategy of the whole MG and how the renewable sources have to react when the PLS is detected is explained in Section 4. The proposed control strategy is verified in Section 5 through hardware-in-the-loop results. This work is concluded in Section 6, where the obtained results are discussed and conclusions are reached.

2. Single-Phase MG Structure and System Configuration

Figure 1 shows a possible single-phase MG connected to the mains through an intelligent transfer switch (ITS). When a fault occurs on the utility grid, the ITS disconnects the MG to enable islanded operation. Then, RES and HESS units are left on their own to supply the loads at nominal voltage and frequency. This MG is formed around a common AC link, to which the HESS, RESs, and loads are directly connected. PV panels are depicted attached to a maximum power point tracker (MPPT) converter, although they could be directly connected to the AC line through the power inverter. Commonly, loads can be practically divided into active and passive ones, but all of them are usually designed for a wide range of input AC voltage, e.g., 100–240 V RMS.

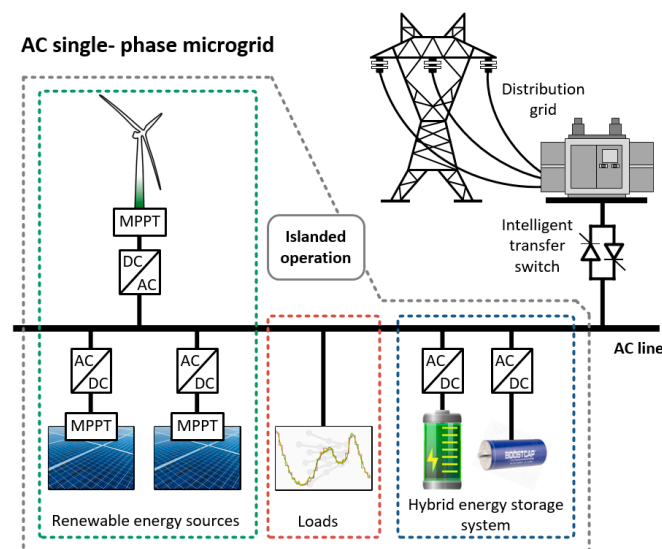


Figure 1. Typical configuration of an AC single-phase microgrid.

As previously mentioned, the energy storage unit fixes both voltage and frequency in the MG during islanded operation, and provides a power buffer, as expressed in (1).

When the *SoC* of the batteries is in a safe region, they can absorb the extra power generated by the RESs that is not consumed by the loads (if there is any), charging up these electrochemical devices.

$$\left. \begin{aligned} P_{HESS} &= P_{BESS} + P_{SESS} \\ P_{HESS} &= \sum_{j=1}^m P_{LOAD_j} - \sum_{i=1}^n P_{RES_i} \end{aligned} \right\} \quad (1)$$

Under these conditions, the RESs operate by injecting all the available power with an MPPT algorithm. Different up to date control strategies have been developed for both PV and wind sources [9,10,33–35]. For this work, the authors have focused their interests on PV technology and the perturb and observe method. Like all MMPT, this algorithm is responsible for finding the operation point where the maximum power from the PV panel can be extracted.

When the batteries are fully charged, a coordinated control strategy is necessary to command the BESS control loop to stop absorbing power and therefore, a new equilibrium point is achieved as expressed in (2):

$$\left. \begin{aligned} P_{HESS} &\approx 0 \\ \sum_{j=1}^m P_{LOAD_j} &\approx \sum_{i=1}^n P_{RES_i} \end{aligned} \right\} \quad (2)$$

Moreover, grid-following units have to reduce their power contribution to match the loads' consumption, shifting from the maximum power point (MPP). This transition must be done smoothly in order to avoid rough transients.

Upon a sudden change in the load conditions, SESS initially provide the required power due to their faster response capability. Therefore, supercapacitors are used to provide/absorb power during the transients. The difference between the reference of the overall power of the HESS and the transient power managed by the SESS is the power reference of the BESS. This strategy ensures an optimal use of both storage technologies, expanding their useful life. Several strategies can be used to split the power share between the SESS and the BESS of the hybrid system. In DC MGs, the most simple way is to obtain the power reference of the batteries by applying a lowpass filter to the overall power reference as shown in (3) [36,37]. In AC MGs, this step is not as straightforward, as discussed in following sections.

$$\left. \begin{aligned} P_{BESS}(s) &= \frac{\omega_c}{s+\omega_c} \cdot P_{HESS}(s) \\ P_{SESS}(s) &= P_{HESS}(s) - P_{BESS}(s) \end{aligned} \right\} \quad (3)$$

3. PLS Concept Applied to Single-Phase MGs

There are some technical papers in the bibliography where the use of PLS is applied to enable communications between converters in a MG. In some of these works, the PLS is applied to DC MGs [18,20,24] where different control strategies can be found. For instance, in [24], the droop profile varies depending on the PLS frequency. This means there is a continuous injection of a sinusoidal signal into the DC bus. On the other hand, in [18] the control strategy is based not only on a droop control, but on keeping the RES units operating at their MPP while the batteries' SoC is in a safe zone. The moment this SoC is high enough to trigger the PLS, the RESs change to a different operation mode. PLS can also be applied to AC power systems (three-phase ones) as proposed in [21,22,25]. In this particular work, the previous ideas are adapted to be used in single-phase small MGs.

3.1. Selection of the PLS Frequency

Figure 2 shows the basic structure of the MG under study. It consists of a master HESS and two slave PV units. The PLS is generated by the BESS and is measured and filtered in the capacitor of the filter of each RES unit. The PLS is triggered when the SoC of the batteries reaches a certain value. Then, it is broadcasted with a certain frequency that increases as the SoC does. The most appropriate frequency range of the PLS has to be studied in order to avoid interactions with key frequencies like the grid, high frequency harmonics, or the bandwidth of the closed loop control of the PLS. In the particular case of [21] and due to sidebands of the injected signal, a frequency of 90 Hz is selected. However, in our case study, there are unknown line impedances that may affect the propagation of the

PLS. Another issue that might disturb this signal is the nature of the loads, i.e., resistive, inductive, and their respective apparent power consumptions. Hence, a frequency analysis of the whole system is required, depending on all these factors and the recommended $f_{PLS_{min}}$ in [21] may not be adequate or at least not the best choice for this particular case.

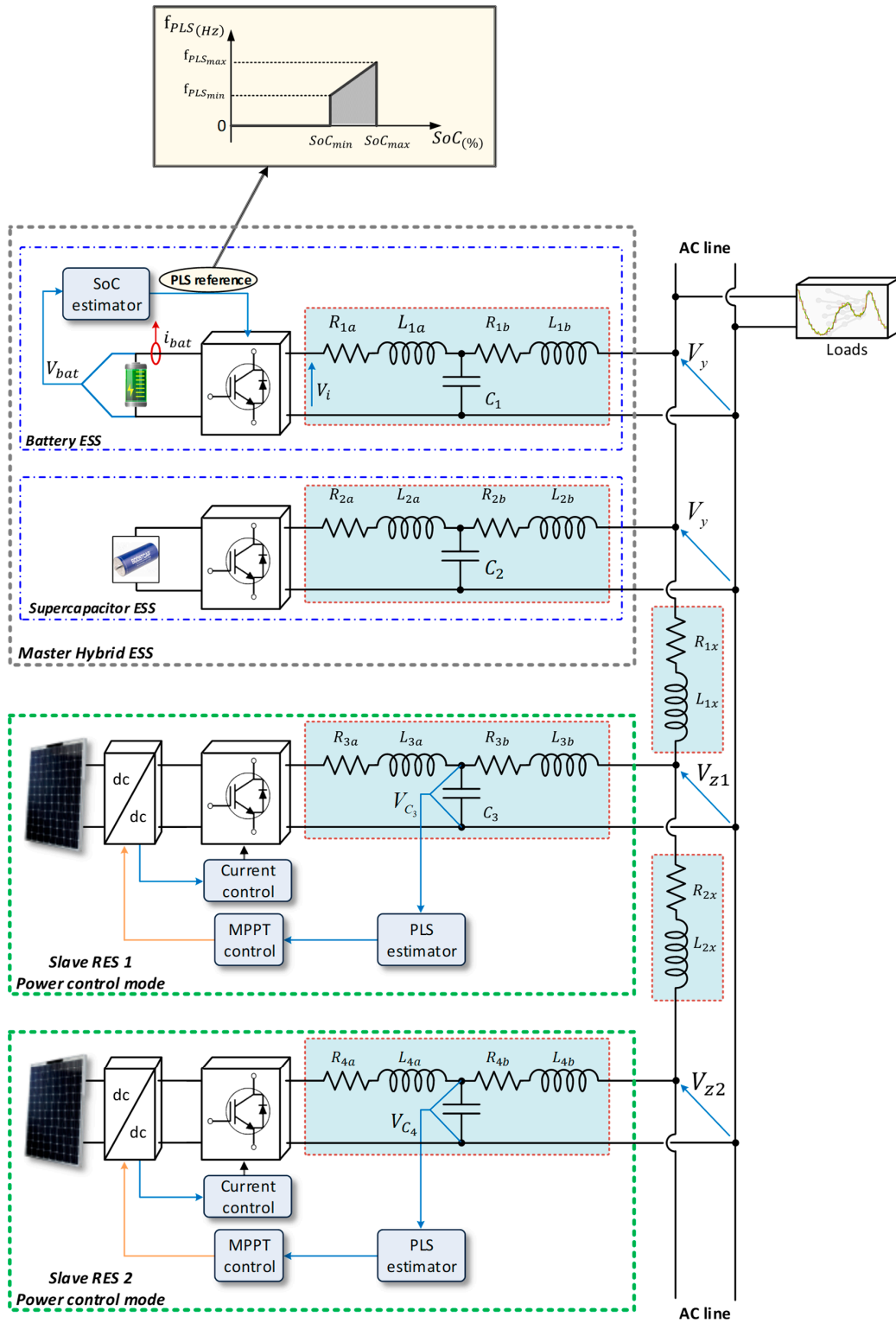


Figure 2. Structure of the AC single-phase microgrid under study.

According to Figure 2, the transfer function between V_{C3} and V_y is denoted by (4):

$$G_{C_3y}(s) = \frac{V_{C_3}(s)}{V_y(s)} = \frac{1}{(L_{3b}C_3s^2 + R_{3b}C_3s) + (L_{1x}C_3s^2 + R_{1x}C_3s) + 1} \quad (4)$$

And the transfer function between V_y and V_{C1} is:

$$G_{yC_1}(s) = \frac{V_y(s)}{V_{C_1}(s)} = \frac{Z}{L_{1b}s + R_{1b} + Z} \quad (5)$$

where Z is the impedance of the load.

The relation between the point where the PLS is injected and the voltage at C_1 is therefore:

$$G_{C_1i}(s) = \frac{V_{C_1}(s)}{V_i(s)} = \frac{1}{L_{1a}C_1s^2 + R_{1a}C_1s + 1} \quad (6)$$

Combining (4), (5) and (6), the transfer function between the voltage at the capacitor of the LCL RES 1 filter and V_i is:

$$G_{C_3i}(s) = \frac{V_{C_3}(s)}{V_i(s)} = G_{C_1i}(s) \cdot G_{yC_1}(s) \cdot G_{C_3y}(s) \quad (7)$$

Once the transfer function of the system is known, the effect of the load and line impedances in the PLS needs to be studied. Figure 3 shows the effect of the load over the attenuation of the PLS signal in a Bode diagram. The effect of a pure resistive load is analyzed in Figure 3a, and the consequences of including an inductive performance can be seen Figure 3b. At low to medium range frequencies, the nature of the load has no significant consequences on the Bode diagram.

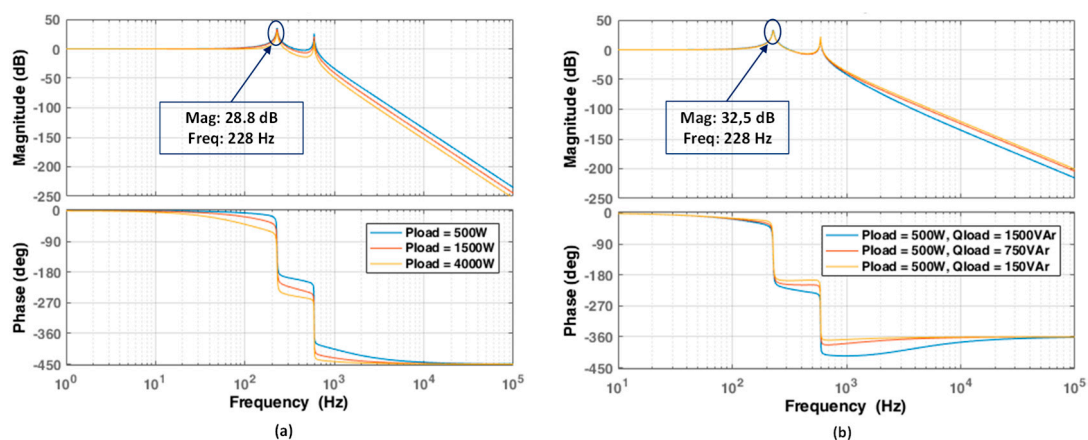


Figure 3. Effect of the load whether it is: (a) resistive (b) inductive.

On the other hand, the effect of line impedances on the PLS attenuation is shown in the Bode diagram of Figure 4. This analysis was performed for several variations in the impedance of the cable.

This very same analysis can be done for the second RES. However, it is necessary to include the corresponding line impedances to obtain the equivalent transfer function as depicted in Figure 5a. The evolution of its root locus is plotted in Figure 5b. The system poles move in different directions depending on those line impedances.

There is a common frequency to all previous analyses that seems suitable to be the PLS one, and that is 228 Hz. This frequency is not affected either by the nature of the load or the line impedances and it is valid for both RES 1 and RES 2 units. This frequency is not close to 100 Hz and it will not interact with the AC loads. Moreover, it is not low enough to disturb the converters' primary control loops. In the particular case of lighting systems, flickering is a key issue. There are some sensitive kinds of lamps (e.g. filament-LED lamps) that could interact with a PLS frequency close to 100 Hz,

resulting in undesired situations. That is why the frequency used in [31] is not recommendable. Thus, this value of 228 Hz has been chosen as the center frequency of the power line signal.

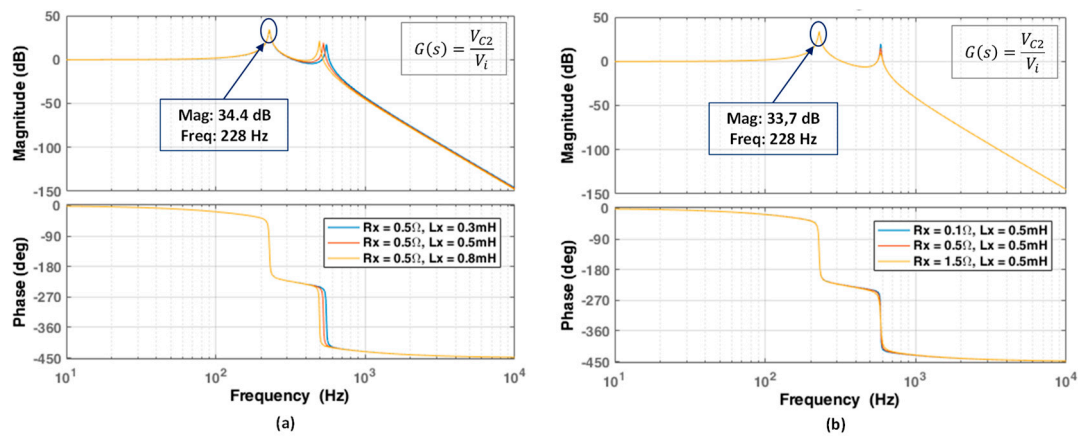


Figure 4. Effect of the line impedances on the power line signaling (PLS) reception at C_3 : (a) analysis of the line inductance. (b) Analysis of the line resistance.

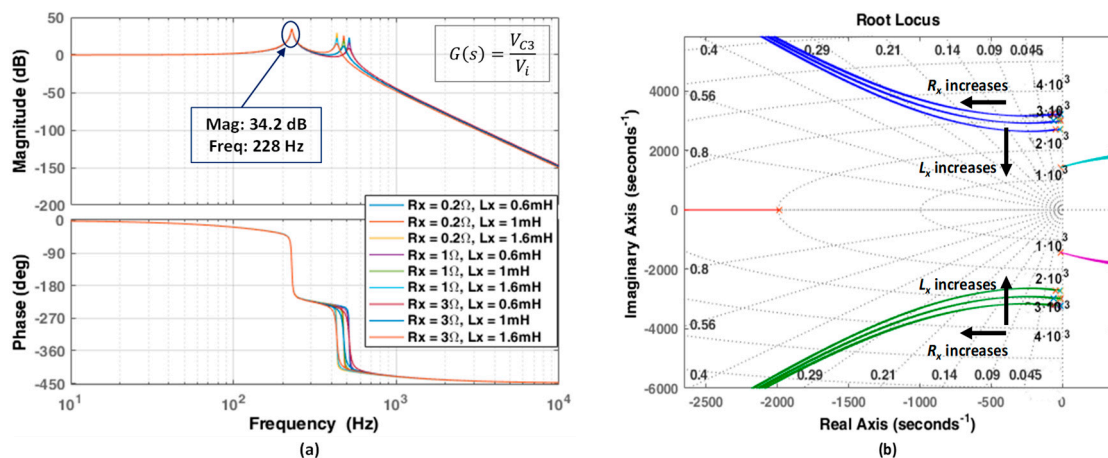


Figure 5. Effect of the line impedances on the PLS reception at C_4 : (a) Bode diagram. (b) root locus.

3.2. Detection of the PLS Frequency

The detection of the PLS is done at the capacitor of the filter of every RES unit attached to the MG. The voltage at these capacitors is measured for two reasons: firstly, to synchronize the grid-following inverter and second, to check if there is any high frequency signal related to communications. As explained in [31], in order to filter possible sidebands, high order filters are required. Choosing a much higher power line frequency signal would have facilitated the filtering process, although it could have interacted with the current loop bandwidth. However, in order to work only with power line signal, two filters are required: a bandstop to attenuate the grid frequency, which has bigger amplitude than the PLS, and a bandpass focused on the objective region (see Figure 6). In this work, Infinite impulse response (IIR) filters have been implemented due to their faster response and fewer coefficients [38].

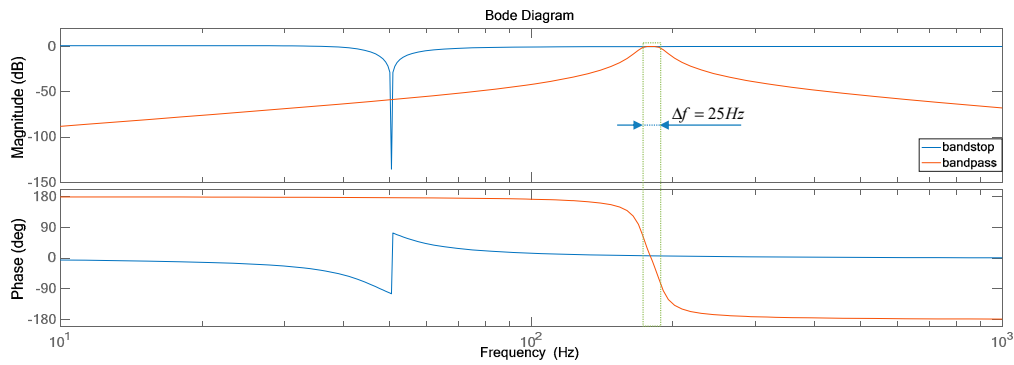


Figure 6. IIR notch and bandpass filters. Bandpass filter order: 4th. Cutting frequencies: 216 Hz, 241 Hz. Sampling rate: 10 kHz.

3.3. PLS Closed-Loop Algorithm

Self-adaptive proportional-resonant (PR) controllers are required for the purpose of ensuring zero steady-state errors of the power line signals. The ideal PR controller has an infinite gain at the AC frequency of ω_{PLS} and no phase shift and gain at other frequencies. By including an anti-windup term and IIR filters, the final control loop of the PLS can be obtained (Figure 7). The PLS signal is generated by a dedicated algorithm that provides the frequency information to the controller, behaving as a self-adaptive one.

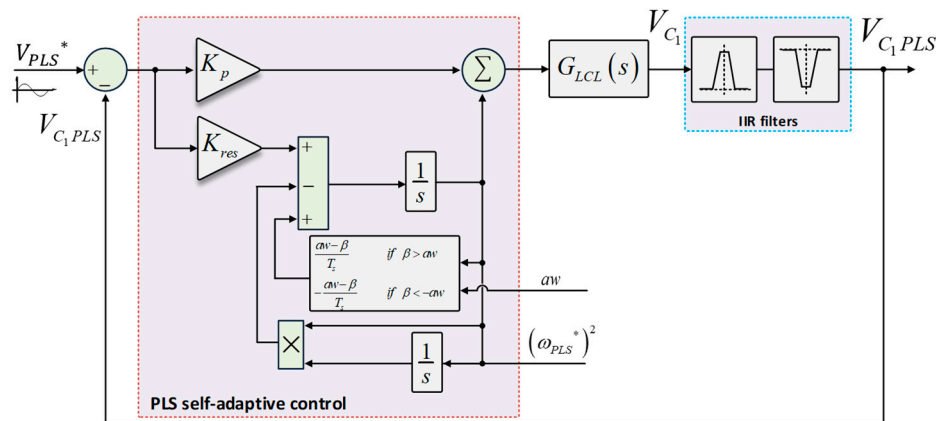


Figure 7. PLS resonant control algorithm.

4. Control Strategy of the MG

The distributed control strategy that prevents batteries from overcharging, as well as maximizing the power contribution of the RESs to the MG, is presented in Figure 8. All different control loops are depicted. A primary control algorithm with two cascade loops for the HESS establishes the MG in a nominal operation point (230 V RMS, 50 Hz). Note how the BESS uses two control loops (voltage and current) to set the MG voltage and frequency, whereas the SESS operates as a grid-following unit, with compensating peak currents. RESs are programmed to inject the maximum power available until power line communications are detected. When that happens, their power contribution is reduced according to the PLS frequency. A simplified flowchart of this algorithm is depicted in Figure 9. This diagram represents the behavior of both HESS and RES units.

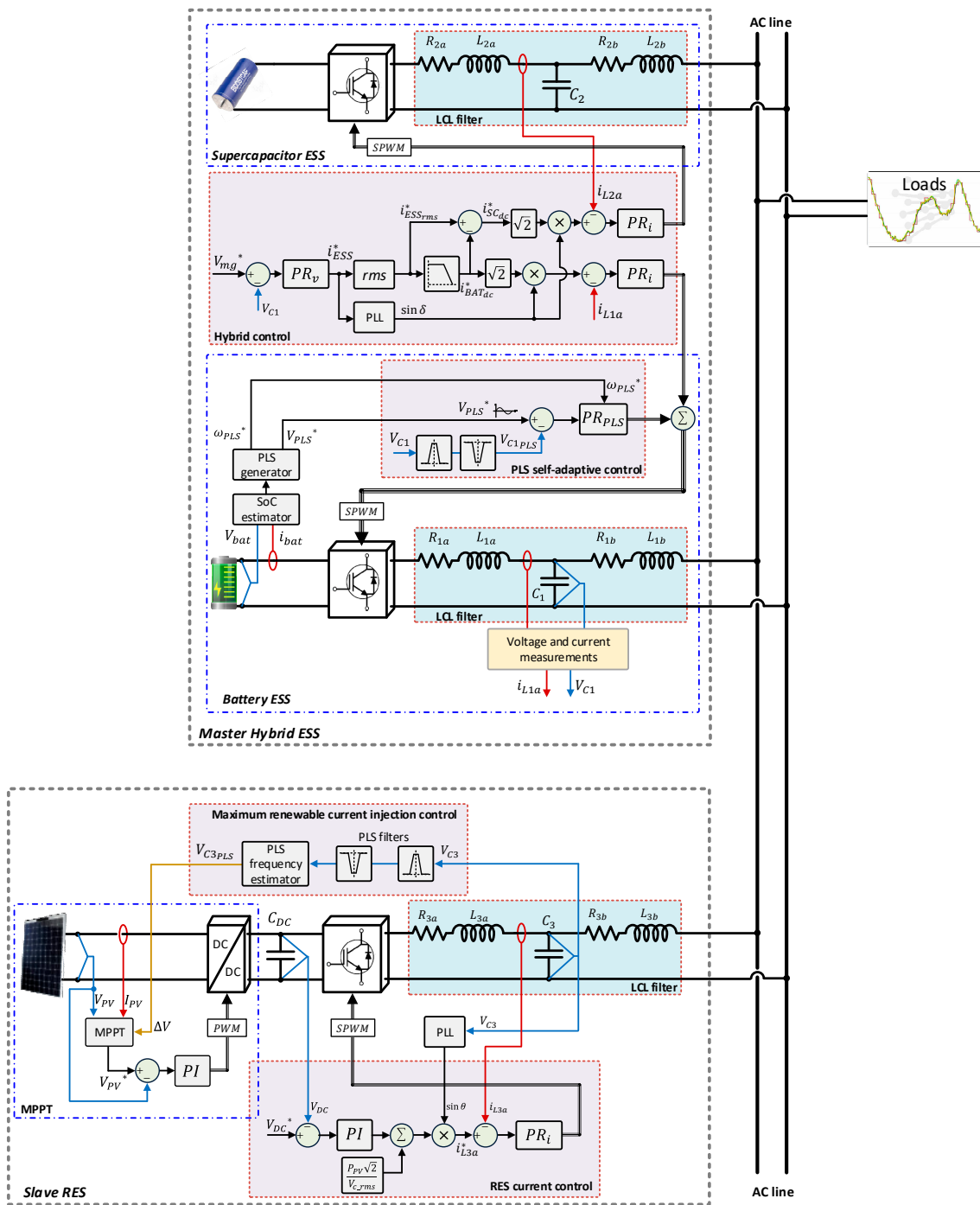


Figure 8. Control diagram of the microgrid (MG).

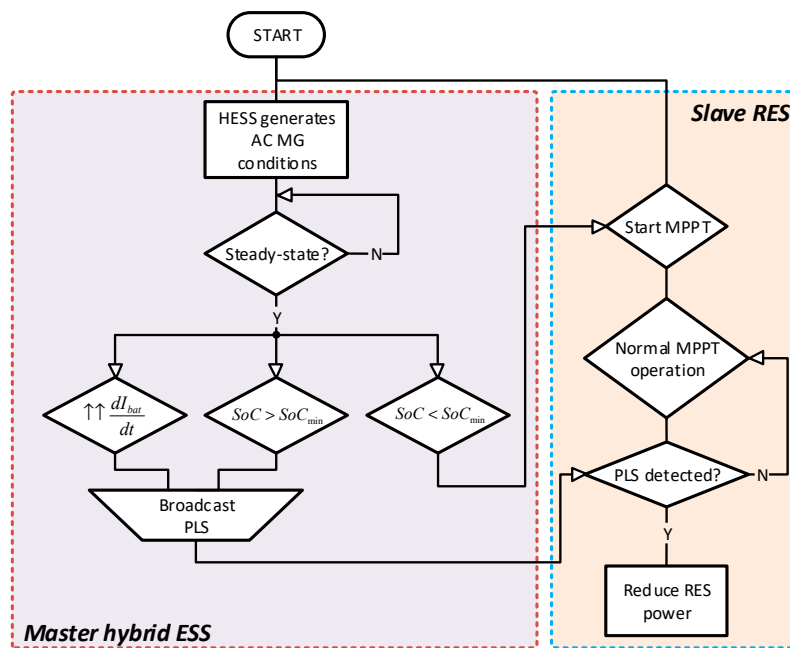


Figure 9. Simplified flowchart of the control algorithm.

4.1. PLS Generation and Event Triggers

The main objective of the PLS communications is the protection of the batteries and therefore, to extend their life. Different events can trigger PLS generation. The primary event that activates communications is a dangerously high SoC of the batteries.

However, there can be other events which could prompt warning signals from the BESS. For instance, a large derivative of the input current into the batteries is not recommended. This could mean there has been an important sudden change in the load or that something is wrong in the MG. When controlling the SoC , the frequency of the PLS is defined by (8):

$$f_{PLS} = \begin{cases} 0 & SoC < SoC_{min} \\ (SoC - SoC_{min}) \cdot m + f_{PLSmin} & SoC_{min} \leq SoC \leq SoC_{max} \end{cases} \quad (8)$$

where m is the slope of the curve depicted in Figure 2.

4.2. PV Slave Unit under Power Control Conditions

The interface of the PV panels can be done in many ways. For instance, in countries with low grid voltages, like Japan, it is becoming very popular to connect the PV panel directly to the grid through an inverter. The MPPT is implemented in the DC-AC inverter [10]. However, the general case is the one depicted in Figure 8, where the MPPT is an independent DC-DC converter that injects the PV current into a DC bus.

This DC link voltage is controlled by the DC-AC inverter. Many MMPT techniques can be found in the bibliography [33–35]. In the present work, a perturb and observe algorithm was used, although it should not be complicated to apply the proposed power control algorithm to any other MPPT technique.

In a safe SoC scenario, the performance of a RES is fixed by the MPPT, providing the maximum available power to the MG. However, if power line communications are detected, the MPPT has to shift the operation point to a different one where the generated power is lower.

The proposed power control algorithm (PLS frequency estimator block in Figure 8) reads the frequency of the PLS and generates a ΔV that shifts the MPP accordingly, generating a new voltage reference to be tracked by the PI controller of the MPPT algorithm. ΔV can be calculated as follows:

$$\Delta V = \begin{cases} 0 & \text{if } f_{PLS} = 0 \\ \left(\frac{V_{oc} - V_{MPP}}{f_{PLS_{max}} - f_{PLS_{min}}} \right) \cdot (f_{PLS} - f_{PLS_{min}}) & \text{if } f_{PLS} \geq f_{PLS_{min}} \end{cases} \quad (9)$$

The previous explanation about shifting the MPP is graphically represented in Figure 10. A red square points out the nominal MPP, i.e., no PLS detected. If there is a PLS broadcast, then the operating point moves to a new one (red circumference), reducing the power obtained from the PV panels. This displacement of the MPP is therefore done according to f_{PLS} .

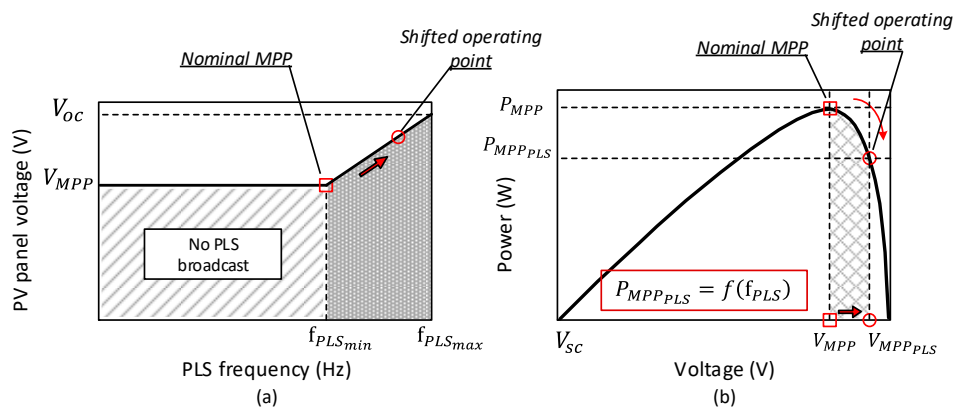


Figure 10. Power control of the photovoltaic (PV) panels when communications are detected. (a) PV panel voltage vs. PLS frequency. (b) PV power vs. PV voltage.

4.3. Grid-Following Unit (RES Inverter)

The grid-following inverter, which operates together with the MPPT, behaves as a current mode voltage source inverter (CM-VSI). It synchronizes with the MG voltage thanks to a dedicated PLL whereas the current reference is tracked by a single PR controller.

4.4. SoC Estimation

Many SoC techniques have been developed during the past few years, allowing users to obtain precise information about remaining battery capacity. Some of these techniques can be found in the bibliography [39–42].

However, these approaches are not easy to reproduce by non-expert researchers. Instead, in this work, a simpler ampere-hour counting method was used to estimate the SoC of the batteries:

$$SoC(t) = SoC(0) - \int_0^t \eta_{bat} \frac{I_{bat}(t)}{C_{bat}} dt \quad (10)$$

where $SoC(0)$ is the initial SoC, C_{bat} is the capacity in Ah, η_{bat} is the charging/discharging efficiency, and I_{bat} is the instantaneous current at the battery [43].

4.5. Plug-and-Play Capability of Additional Units

According to Figure 5, a new RES unit connected to the MG does not affect or damage communications if it is not located far away from the HESS. This unit should be treated the same way as the already-present RES functional units. Therefore, plug-and-play capability can be easily achieved for new RES structures if the proposed control algorithm is adopted.

Nevertheless, in the case of a generic ESS (HESS, BESS, SESS), one should develop a different approach. An interesting strategy would be to operate this second ESS as a backup unit. If the main HESS fails, a second equipment can restore the MG conditions, as an uninterruptible power supply (UPS). There is another option, though, and that is to operate this new unit in parallel with the master HESS, providing a secondary control of frequency and voltage [44], or following a particular droop control [45].

5. Hardware-in-the-Loop Results

The proposed control strategy has been verified through hardware-in-the-loop simulations on a Speedgoat[®] platform. The parameters of the MG have been gathered in Table 1. One HESS and two PV RES units were simulated supplying different load steps.

Table 1. Power stage and control parameters.

Parameter	Symbol	Value
HESS		
Nominal MG voltage	V_{MG}	230 V
Nominal MG frequency	f_{MG}	50 Hz
Filter inductances	L_a, L_b	1.8 mH
Filter capacitance	C_1, C_2	27 μ F
Voltage control inner loop	K_{p_v}, K_{res_v}	0.1, 10
Current control inner loop	K_{p_i}, K_{res_i}	10, 1500
Lower-threshold of SoC	SoC_{min}	95%
Minimum PLS frequency	$f_{PLS\ min}$	226 Hz
Maximum PLS frequency	$f_{PLS\ max}$	231 Hz
PLS control loop	K_{p_PLS}, K_{res_PLS}	5, 250
RES		
Filter inductances	L_a, L_b	1.8 mH
Filter capacitance	C_3, C_4	4 μ F
Current control inner loop	K_{p_i}, K_{res_i}	30, 500
Load Steps		
Load 1 ($t = 0s$)	-	1500 W
Load 2 ($t = 55s$)	-	2500 W
Load 3 ($t = 70s$)	-	2500 W
Load 3 ($t = 85s$)	-	-2500 W

These simulation results can be found in Figure 11. According to Figure 9, during the start up of the system, only the HESS is able to supply the loads. Therefore, up to $t = 5$ s, the batteries are discharging and the PV panels are not operative. Beyond that point, RES units begin to inject power into the MG, and therefore, the power contribution of the BESS is continuously reduced until $t \approx 11$ s, when the BESS starts to absorb energy and thus, charge the batteries. The SoC of those batteries is climbing under safe values until $t \approx 38$ s. At that point, it reaches the 95% of its nominal value and PLS is broadcasted. Therefore, the RES units commence to shift the operating point from the MPP, and hence reduce their power contribution.

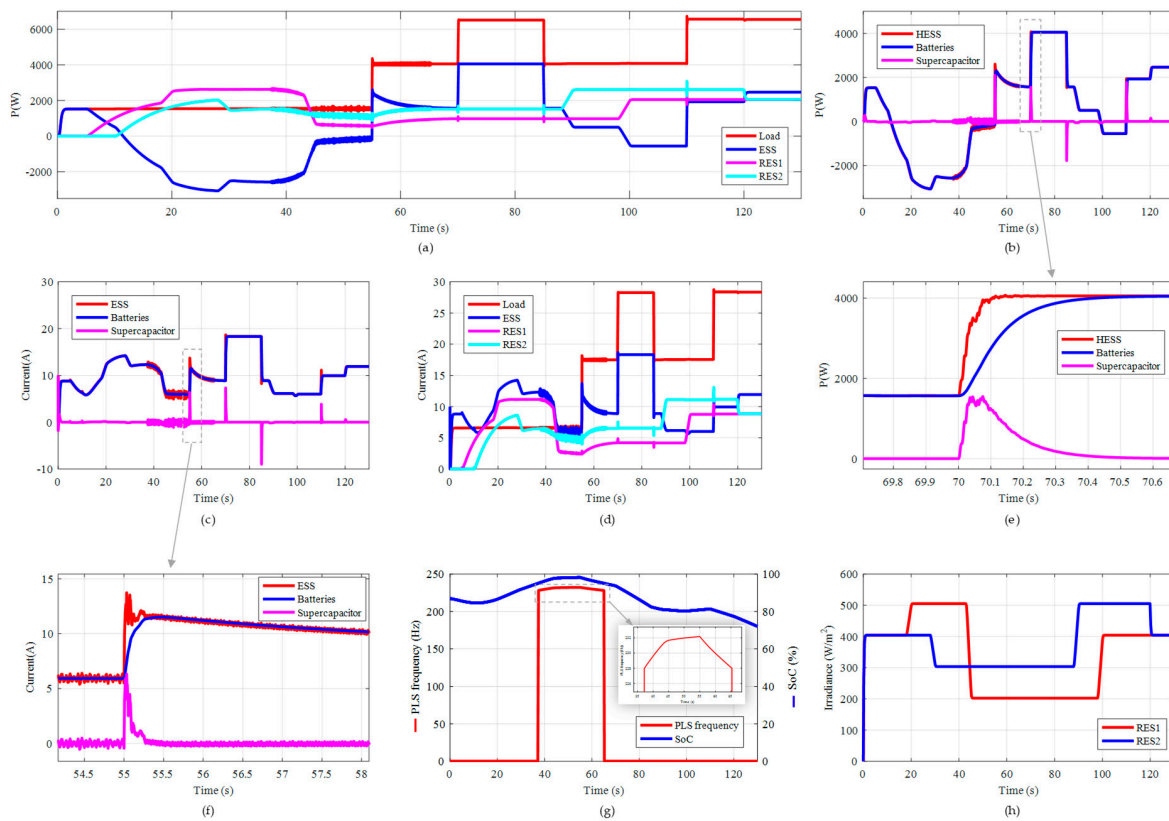


Figure 11. Simulation results: (a) Distribution of the powers in the MG. (b) Power contribution of the hybrid energy storage system (HESS). (c) HESS rms currents. (d) Distribution of the rms currents in the MG. (e) Detailed view of the HESS powers at $t = 70$ s. (f) Detailed view of the HESS rms currents at $t = 55$ s. (g) State of charge of the batteries and PLS frequency. (h) Irradiance on PV panels.

Three load steps can be found in the simulation results at different moments as summarized in Table 1 (Figure 11a summarizes all these load steps and their effect on the power converters). A new scenario appears at $t = 55$ s when a 2500 W load is connected. The SESS have higher bandwidth and thus it is able to respond faster to this variation. The BESS follows this change of the consumption trend more slowly. Therefore, this transition is assumed by the HESS, while the frequency of the PLS is reduced due to the equivalent SoC decrease. The RES are less limited by the PLS, and therefore they will look for a new operation point.

This operating point remains stable until there is a new change in the MG conditions. The SoC of the batteries gradually decreases and at $t \approx 65$ s it goes below the SoC_{min} . Power-line communications are thus shut down and RES units again inject all the available power into the MG. This situation remains steady for a few seconds, but then a new load is connected at $t = 70$ s. Again, the SESS is the first unit to react to this transient and the BESS contributes with a softer current reference (Figures 11b and 11e show the power contribution of both SESS and BESS, as well as a more detailed view of the transient at $t = 70$ s).

The MPPT algorithm has been also tested, as can be observed in Figure 11h. The irradiance over both RES units changes during the simulation. The MPPT perfectly tracks the irradiance over the PV panels.

6. Conclusions

In this paper, a distributed control strategy for islanded single-phase microgrids with hybrid energy storage systems based on power line communications has been presented. This approach allows for a coordinated power regulation between the variety of distributed generators and loads that can be encountered in a microgrid. The physical configuration of the microgrid and how to apply power

line communications in single-phase islanded microgrids have been studied. The attenuation of this kind of communications can be altered by the integration of more power converters (renewable energy sources, power loads, etc.) and by line impedances, and thus the most suitable range of frequencies for the communications has been calculated.

The proposed control strategy has been validated through hardware-in-the-loop simulations. The renewable energy sources inject power into the microgrid depending on the SoC of the batteries of the hybrid energy storage system. When a reference is reached, the grid-following units reduce their power contribution by shifting the operating point in the MPPT algorithm. This displacement of the maximum power point is done according to the frequency of the communication signal. Upon sudden changes in the load conditions, the PV panels again shift their operation point if they are required to.

The calculation of the current references of both systems that make up the hybrid system has been studied. The supercapacitor is responsible for absorbing or delivering the power peaks, while the batteries follow a less aggressive charge/discharge profile. In this way, it is possible to increase its useful life.

Author Contributions: The research study was carried out successfully with contribution from all authors.

Funding: This work has been supported by the Ministry of Economy and Competitiveness of the Government of Spain (MINECO), the Government of the Principality of Asturias and the European Union through the European Regional Development Fund (ERFD), under Research Grants ENE2013-41491-R (LITCITY Project) and GRUPIN14-076.

Acknowledgments: The authors would like to thank Dan Wu, Nelson Diaz, Lexuan Meng, Juan Carlos Vasquez, Francisco Juarez, Alejandro Suarez, Emilio L. Corominas, Manuel Rico and Pablo Garcia for their valuable contributions.

Conflicts of Interest: The authors declare no conflict of interest.

List of Acronyms

BESS	Battery Energy Storage System
DG	Distributed Generator
ESS	Energy Storage System
HESS	Hybrid Energy Storage System
IRR	Infinite impulse response (filter)
ITS	Intelligent Transfer Switch
MG	Microgrid
MPPT	Maximum Power Point Tracker
PLL	Phase-Locked Loop
PLS	Power-Line Signal
PR	Proportional Resonant (controller)
PV	Photovoltaic (panel)
RES	Renewable Energy Source
SESS	Supercapacitor Energy Storage System
SoC	State of Charge

References

1. Lasseter, R.H. MicroGrids. In Proceedings of the 2002 IEEE Power Engineering Society Winter Meeting, New York, NY, USA, 1 January 2002; pp. 305–308. [\[CrossRef\]](#)
2. Lopes, J.A.P.; Moreira, C.L.; Madureira, A.G. Defining control strategies for microgrids islanded operation. *IEEE Trans. Power Syst.* **2006**, *21*, 916–924. [\[CrossRef\]](#)
3. Guerrero, J.M.; Vasquez, J.C.; Matas, J.; De Vicuña, L.G.; Castilla, M. Hierarchical control of droop-controlled AC and DC microgrids—A general approach toward standardization. *IEEE Trans. Ind. Electron.* **2011**, *58*, 158–172. [\[CrossRef\]](#)
4. Guerrero, J.M.; Chandorkar, M.; Lee, T.; Loh, P.C. Advanced control architectures for intelligent microgrids; Part I: Decentralized and hierarchical control. *IEEE Trans. Ind. Electron.* **2013**, *60*, 1254–1262. [\[CrossRef\]](#)

5. Rocabert, J.; Luna, A.; Blaabjerg, F.; Paper, I. Control of power converters in AC microgrids. *IEEE Trans. Power Electron.* **2012**, *27*, 4734–4749. [CrossRef]
6. Su, W.; Eichi, H.; Zeng, W.; Chow, M.Y. A Survey on the electrification of transportation in a smart grid environment. *IEEE Trans. Ind. Inf.* **2012**, *8*, 1–10. [CrossRef]
7. Blaabjerg, F.; Teodorescu, R.; Liserre, M.; Timbus, A.V. Overview of control and grid synchronization for distributed power generation systems. *IEEE Trans. Ind. Electron.* **2006**, *53*, 1398–1409. [CrossRef]
8. Shahidehpour, M. Don't let the sun go down on PV. *Energy* **2004**, *2*, 40–48. [CrossRef]
9. Koutroulis, E.; Kalaitzakis, K. Design of a maximum power tracking system for wind-energy-conversion applications. *IEEE Trans. Ind. Electron.* **2006**, *53*, 486–494. [CrossRef]
10. Teodorescu, R.; Liserre, M.; Rodriguez, P. Photovoltaic inverter structures. In *Grid Converters for Photovoltaic and Wind Power Systems*; Wiley-IEEE Press: New York, NY, USA, 2011; pp. 5–29. ISBN 978-0-470-05751-3.
11. Rico-Secades, M.; Calleja, A.; Llera, D.G.; Corominas, E.L.; Medina, N.H.; Miranda, J.C. Cosine Phase Droop Control (CPDC) for the dual-active bridge in lighting smart grids applications. In Proceedings of the 2016 IEEE International Conference on Industrial Technology (ICIT), Taipei, China, 14–17 March 2016; pp. 411–418. [CrossRef]
12. Nehrir, M.H.; Wang, C.; Strunz, K.; Aki, H.; Ramakumar, R.; Bing, J.; Miao, Z.; Salameh, Z. A review of hybrid renewable/alternative energy systems for electric power generation: Configurations, control, and applications. *IEEE Trans. Sustain. Energy* **2011**, *2*, 392–403. [CrossRef]
13. Engler, A. Control of parallel operating battery inverters. *Photovolt. Hybrid Power Syst. Conf.* [CD-ROM]. 2000.
14. Stroe, D.I.; Swierczynski, M.; Stroe, A.I.; Laerke, R.; Kjaer, P.C.; Teodorescu, R. Degradation behavior of lithium-ion batteries based on lifetime models and field measured frequency regulation mission profile. *IEEE Trans. Ind. Appl.* **2016**, *52*, 5009–5018. [CrossRef]
15. Zhao, B.; Zhang, X.; Chen, J.; Wang, C.; Guo, L. Operation optimization of standalone microgrids considering lifetime characteristics of battery energy storage system. *IEEE Trans. Sustain. Energy* **2013**, *4*, 934–943. [CrossRef]
16. Fitri, I.; Kim, J.-S.; Song, H. A robust suboptimal current control of an interlink converter for a hybrid AC/DC microgrid. *Energies* **2018**, *11*, 1382. [CrossRef]
17. Asghar, F.; Talha, M.; Kim, S.H. Robust frequency and voltage stability control strategy for standalone AC/DC hybrid microgrid. *Energies* **2017**, *10*, 760. [CrossRef]
18. Pan, H.; Ding, M.; Chen, A.; Bi, R.; Sun, L.; Shi, S. Research on distributed power capacity and site optimization planning of AC/DC hybrid micrograms considering line factors. *Energies* **2018**, *11*, 1930. [CrossRef]
19. Baek, J.; Choi, W.; Chae, S. Distributed control strategy for autonomous operation of hybrid AC/DC microgrid. *Energies* **2017**, *10*, 373. [CrossRef]
20. Both, J. The modern era of aluminum electrolytic capacitors. *IEEE Electr. Insul. Mag.* **2015**, *31*, 24–33. [CrossRef]
21. Rubycon Corporation. Aluminum Electrolytic Capacitor Technical Notes. Available online: <http://www.rubycon.co.jp/en/products/alumi/technote5.html> (accessed on 1 December 2018).
22. Spanik, P.; Frivaldsky, M.; Kanovsky, A. Life time of the electrolytic capacitors in power applications. In Proceedings of the 12th International Conference ELEKTRO 2014, Rajecke Teplice, Slovakia, 19–20 May 2014; pp. 233–238.
23. Shrivastava, A.; Azarian, M.H.; Pecht, M. Failure of polymer aluminum electrolytic capacitors under elevated temperature humidity environments. *IEEE Trans. Compon. Packag. Manuf. Technol.* **2017**, *7*, 745–750. [CrossRef]
24. Sun, B.; Fan, X.; Qian, C.; Zhang, G. PoF-Simulation-assisted reliability prediction for electrolytic capacitor in LED drivers. *IEEE Trans. Ind. Electron.* **2016**, *63*, 6726–6735. [CrossRef]
25. Byeon, G.; Yoon, T.; Oh, S.; Jang, G. Energy management strategy of the DC distribution system in buildings using the EV service model. *IEEE Trans. Power Electron.* **2013**, *28*, 1544–1554. [CrossRef]
26. Kim, J.Y.; Jeon, J.H.; Kim, S.K.; Cho, C.; Park, J.H.; Kim, H.M.; Nam, K.Y. Cooperative control strategy of energy storage system and microsources for stabilizing the microgrid during islanded operation. *IEEE Trans. Power Electron.* **2010**, *25*, 3037–3048. [CrossRef]

27. Wu, D.; Tang, F.; Dragicevic, T.; Vasquez, J.C.; Guerrero, J.M. A control architecture to coordinate renewable energy sources and energy storage systems in islanded microgrids. *IEEE Trans. Smart Grid* **2015**, *6*, 1156–1166. [[CrossRef](#)]
28. Dragievic, T.; Guerrero, J.M.; Vasquez, J.C. A distributed control strategy for coordination of an autonomous LVDC microgrid based on power-line signaling. *IEEE Trans. Ind. Electron.* **2014**, *61*, 3313–3326. [[CrossRef](#)]
29. Sun, K.; Zhang, L.; Xing, Y.; Guerrero, J.M. A distributed control strategy based on DC bus signaling for modular photovoltaic generation systems with battery energy storage. *IEEE Trans. Power Electron.* **2011**, *26*, 3032–3045. [[CrossRef](#)]
30. Schönberger, J.; Duke, R.; Round, S.D. DC-bus signaling: A distributed control strategy for a hybrid renewable nanogrid. *IEEE Trans. Ind. Electron.* **2006**, *53*, 1453–1460. [[CrossRef](#)]
31. Tuladhar, A.; Jin, H.; Unger, T.; Mauch, K. Control of parallel inverters in distributed AC power systems with consideration of line impedance effect. *IEEE Trans. Ind. Appl.* **2000**, *36*, 131–138. [[CrossRef](#)]
32. Wu, D.; Tang, F.; Dragicevic, T.; Vasquez, J.C.; Guerrero, J.M. Autonomous active power control for islanded AC microgrids with photovoltaic generation and energy storage system. *IEEE Trans. Energy Convers.* **2014**, *29*, 882–892. [[CrossRef](#)]
33. De Brito, M.A.G.; Galotto, L.; Sampaio, L.P.; De Azevedo Melo, G.; Canesin, C.A. Evaluation of the main MPPT techniques for photovoltaic applications. *IEEE Trans. Ind. Electron.* **2013**, *60*, 1156–1167. [[CrossRef](#)]
34. Abdelsalam, A.K.; Massoud, A.M.; Ahmed, S.; Enjeti, P.N. High-performance adaptive Perturb and observe MPPT technique for photovoltaic-based microgrids. *IEEE Trans. Power Electron.* **2011**, *26*, 1010–1021. [[CrossRef](#)]
35. Subudhi, B.; Pradhan, R. A comparative study on maximum power point tracking techniques for photovoltaic power systems. *IEEE Trans. Sustain. Energy* **2013**, *4*, 89–98. [[CrossRef](#)]
36. Wang, C.S.; Li, W.; Wang, Y.F.; Han, F.Q.; Meng, Z.; Li, G.D. An isolated three-port bidirectional DC-DC converter with enlarged ZVS region for HESS applications in DC microgrids. *Energies* **2017**, *10*, 446. [[CrossRef](#)]
37. Georgious, R.; Garcia, J.; Garcia, P.; Navarro-Rodriguez, A. A comparison of non-isolated high-gain three-port converters for hybrid energy storage systems. *Energies* **2018**, *11*, 658. [[CrossRef](#)]
38. Signal, I.; Magazine, P. What are genetic algorithms? Optimization algorithms. *IEEE Signal Process. Mag.* **1996**, 22–37. [[CrossRef](#)]
39. Bhangu, B.S.; Bentley, P.; Stone, D.A.; Bingham, C.M. Nonlinear observers for predicting state-of-charge and state-of-health of lead-acid batteries for hybrid-electric vehicles. *IEEE Trans. Veh. Technol.* **2005**, *54*, 783–794. [[CrossRef](#)]
40. Coleman, M.; Lee, C.K.; Zhu, C.; Hurley, W.G. State-of-charge determination from EMF voltage estimation: Using impedance, terminal voltage, and current for lead-acid and lithium-ion batteries. *IEEE Trans. Ind. Electron.* **2007**, *54*, 2550–2557. [[CrossRef](#)]
41. Charkhgard, M.; Farrokhi, M. State-of-charge estimation for lithium-ion batteries using neural networks and EKF. *IEEE Trans. Ind. Electron.* **2010**, *57*, 4178–4187. [[CrossRef](#)]
42. He, H.; Xiong, R.; Zhang, X.; Sun, F.; Fan, J. State-of-charge estimation of the lithium-ion battery using an adaptive extended kalman filter based on an improved thevenin model. *IEEE Trans. Veh. Technol.* **2011**, *60*, 1461–1469. [[CrossRef](#)]
43. Díaz, N.L.; Luna, A.C.; Vasquez, J.C.; Guerrero, J.M. Centralized control architecture for coordination of distributed renewable generation and energy storage in islanded AC microgrids. *IEEE Trans. Power Electron.* **2017**, *32*, 5202–5213. [[CrossRef](#)]
44. Simpson-Porco, J.; Shafiee, Q.; Dörfler, F.; Vasquez, J.C.; Guerrero, J.M.; Bullo, F. Secondary frequency and voltage control of islanded microgrids via distributed averaging. *IEEE Trans. Ind. Electron.* **2015**, *62*, 7025–7038. [[CrossRef](#)]
45. Che, L.; Shahidehpour, M.; Alabdulwahab, A.; Al-Turki, Y. Hierarchical coordination of a community microgrid with AC and DC microgrids. *IEEE Trans. Smart Grid* **2015**, *6*, 3042–3051. [[CrossRef](#)]

